iScience

CellPress
OPEN ACCESS

Article

Targeting the mRNA endonuclease CPSF73 inhibits breast cancer cell migration, invasion, and self-renewal

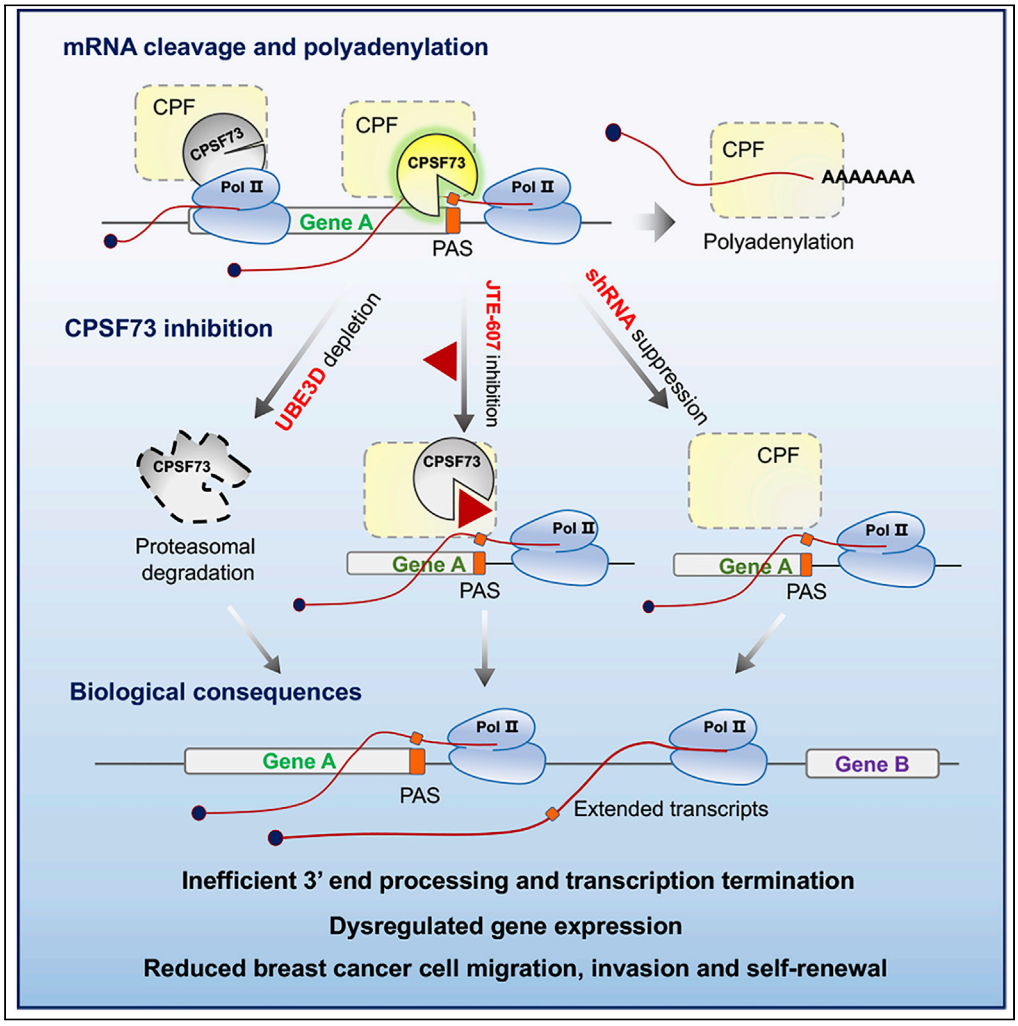

Huiyun Liu, Daniel Heller-Trulli, Claire L. Moore

claire.moore@tufts.edu

Highlights

UBE3D regulates CPSF73 in a conserved way as is found for its yeast homolog

UBE3D stabilizes CPSF73 by protecting it from ubiquitin-mediated degradation

UBE3D regulates breast cancer cell migration and invasion through CPSF73

The level of CPSF73 correlates with breast cancer cell self-renewal properties

Liu et al., iScience 25, 104804
August 19, 2022
https://doi.org/10.1016/j.isci.2022.104804

iScience

CellPress
OPEN ACCESS

Article

Targeting the mRNA endonuclease CPSF73 inhibits breast cancer cell migration, invasion, and self-renewal

Huiyun Liu,[1,2] Daniel Heller-Trulli,[1,2] and Claire L. Moore[1,3,*]

SUMMARY

Cleavage by the endonuclease CPSF73 and polyadenylation of nascent RNA is an essential step in co-transcriptional mRNA maturation. Recent work has surprisingly identified CPSF73 as a promising drug target for inhibiting the growth of specific cancers, triggering further studies on understanding CPSF73 regulation and functions in cells. Here, we report that a HECT-like E3 ligase, UBE3D, participates in stabilizing CPFS73 protein by preventing its ubiquitin-mediated degradation by the proteasome. Depletion of *UBE3D* leads to CPSF73 downregulation, a pre-mRNA cleavage defect, and dysregulated gene expression in cells. UBE3D dysfunction or chemical inactivation of CPSF73 inhibited migration and invasion as well as stem cell renewal phenotypes *in vitro* in triple-negative breast cancer cells. In addition, genetic overexpression of CPSF73 promoted breast cancer stemness and knocking down CPSF73 inhibited stem cell renewal properties. Together, our findings indicate that targeting the pre-mRNA processing nuclease CPSF73 has potential for breast cancer therapy.

INTRODUCTION

Precursor mRNA (pre-mRNAs), which are the primary products resulting from the transcription of protein-coding genes, undergo a series of chemical modifications to form the mature mRNA that is exported to the cytoplasm and translated into the corresponding protein. Key mRNA processing steps include 5′ end capping, removal of introns by splicing, cleavage of mRNA at the 3′ end, and the addition of a long chain of adenine nucleotides known as the poly(A) tail. RNA processing has long been recognized as a means to regulate gene expression, and the abnormal processing of pre-mRNA through alternative splicing and alternative polyadenylation can also initiate cancer and drive tumor progression (Bonnal et al., 2020; Gruber and Zavolan, 2019). These studies make targeting mRNA processing an intriguing anti-cancer strategy (Desterro et al., 2020).

Cleavage and polyadenylation of nascent transcripts is a fundamental process for eukaryotic mRNA maturation and the production of different mRNA isoforms. Through this mechanism, all animal cell mRNAs except those encoding histones receive a 3′ poly(A) tail which protects the mRNA from degradation (Chen and Shyu, 2011), aids in the export of the mature mRNA to the cytoplasm (Stewart, 2019), and binds proteins involved in initiating translation (Moore and von Lindern, 2018). The processing is carried out by machinery that recognizes conserved sequence elements around the cleavage site and is composed of 15 core proteins consisting of the poly(A) polymerase and four complexes (Ren et al., 2020; Sun et al., 2020; Zhang et al., 2020): Cleavage and Polyadenylation Specificity Factor (CPSF), Cleavage Stimulation Factor (CstF), and mammalian Cleavage Factors I (CFIm) and II (CFIIm). Abnormal mRNA 3′ end profiles found in cancer are caused at least in part by changes in the expression levels of components of the cleavage and polyadenylation machinery (Abadi et al., 2019; Chen et al., 2021; Komini et al., 2021; Lin et al., 2021).

A critical component of the processing complex is the essential endonuclease CPSF73. Cleavage by CPSF73 is necessary to provide a substrate for poly(A) polymerase. Without CPSF73's cleavage activity, mRNAs cannot be polyadenylated and released from the site of transcription for export to the cytoplasm. Cleavage by CPSF73 is also necessary for the termination of transcription that defines gene boundaries, and thus inhibits transcriptional interference at downstream genes. Several studies have associated CPSF73 activity with cancer phenotypes (reviewed by (Liu and Moore, 2021)). It has been proposed as a

[1]Department of Developmental, Molecular and Chemical Biology, Tufts University School of Medicine, Boston, MA 02111, USA

[2]These authors contributed equally

[3]Lead contact

*Correspondence: claire.moore@tufts.edu

https://doi.org/10.1016/j.isci.2022.104804

promising biomarker for cancer outcomes (Ning et al., 2019), and its activity is inhibited by the tumor suppressor protein CSR1 but activated by lncRNA CASC9 (Luo et al., 2019; Zhu et al., 2009). Furthermore, small molecule inhibitors of CPSF73 have therapeutic potential for treating specific cancers, inflammatory diseases, and protozoan infections (Liu and Moore, 2021).

Given the central role of CPSF73 for mRNA processing and its implications in therapeutics, it is important to define how it is regulated in order to completely decode its function in cells. Our previous studies showed that Ysh1, the yeast CPSF73 homolog, is a target for ubiquitin-mediated proteasomal degradation. Mechanistically, ubiquitination of Ysh1 is modulated by the presence of Ipa1, an essential protein that physically interacts with Ysh1 and Mpe1, another cleavage/polyadenylation complex subunit (Costanzo et al., 2016; Hill et al., 2019). Mutation of *Ipa1* causes the degradation of Ysh1 by the proteasome (Lee et al., 2020), defects in mRNA 3' end processing *in vitro*, lengthening of mRNAs *in vivo*, and inefficient transcription termination downstream of poly(A) sites (PAS) and at snoRNA genes (Costanzo et al., 2016; Pearson et al., 2019). However, the post-translational regulation of CPSF73 levels in human cells has not been documented. Interestingly, two independent quantitative proteomics screens identified the human Ipa1 homolog, UBE3D, as a CPSF73 interactor (Hein et al., 2015; Huttlin et al., 2017), and CPSF73 was found to be part of the ubiquitome (Chen et al., 2014). Based on these observations, we hypothesized that the mechanism by which Ipa1 regulates polyadenylation may be conserved in humans.

To test our hypothesis, we generated a *UBE3D* KO line in HEK293 cells and found that among the cleavage/polyadenylation core factors, CPSF73 protein, but not its mRNA, was specifically downregulated. CPSF73 is less stable in *UBE3D*-depleted cells, and the degradation of CPSF73 utilized the ubiquitin-proteasome pathway. CPSF73 downregulation mediated by *UBE3D* depletion caused 3′ end processing defects in both HEK293 and the triple-negative breast cancer MDA-MB-231 cell lines. Additional functional studies showed CPSF73 dysfunction mediated by either *UBE3D* depletion or chemical inhibition resulted in the reduction of breast cancer cell migration, invasion, and self-renewal. Furthermore, direct knockdown of *CPSF73* mRNAs effectively suppressed breast cancer cell self-renewal while overexpression of CPSF73 promoted it, highlighting the potential of inhibiting mRNA 3′ end processing in breast cancer therapeutics.

RESULTS

UBE3D regulates CPSF73 at the post-translational level

UBE3D is a HECT-like E3 ligase that has been implicated in cell cycle regulation (Hundley et al., 2021; Kobirumaki et al., 2005), age-related macular degeneration (Huang et al., 2015; Xia et al., 2020), the inflammatory condition of aggressive juvenile periodontitis (Offenbacher et al., 2016), and alterations in the fatty acid profile of muscle (Rovadoscki et al., 2018), but its functional role in mammalian cells has not been determined. Although UBE3D was identified as a CPSF73 interactor in HEK293 and HeLa cells (Hein et al., 2015; Huttlin et al., 2017), how CPSF73 might be regulated by UBE3D is not known. We generated a HEK293 *UBE3D* knockout (KO) cell line using CRISPR-Cas9 technology (Ran et al., 2013). *UBE3D* depletion in the KO cell line was verified both at the genomic level (Figure S1A) and protein level (Figure 1A). To test if CPSF73 was specifically regulated by UBE3D as we observed with their homologs in yeast, we tested the protein levels of core cleavage/polyadenylation (C/P) factors in *UBE3D* KO cells. CPSF73, but not other C/P subunits, was decreased dramatically in *UBE3D* KO cells (Figure 1B), and this regulation was also observed in *UBE3D* knockdown cells (Figures S1B and S1C). Furthermore, the CPSF73 level was rescued by overexpression of UBE3D protein in KO cells (Figure 1B), suggesting that UBE3D is important for maintaining the CPSF73 protein level in human cells. These data also indicate that UBE3D is the likely human homolog of Ipa1 and that its function is conserved across eukaryotes.

To further understand the level at which UBE3D regulated CPSF73, we measured the *CPSF73* mRNA levels in the *UBE3D* wild-type (WT), KO, and addback cells and observed no change among the groups (Figure 1C), suggesting that *UBE3D* depletion does not affect transcription or stability of *CPSF73* mRNAs and that the decrease in CPSF73 protein might be owing to post-translational regulation. To test this hypothesis, we employed a cycloheximide chase assay (Kao et al., 2015) to analyze the stability of CPSF73 in *UBE3D* WT and KO cells. Compared to WT cells, the depletion of *UBE3D* accelerated CPSF73 degradation after blocking protein translation with cycloheximide (Figure 1D), verifying the post-translational regulation of CPSF73 by UBE3D. To assess whether the ubiquitin-proteasome pathway was involved in CPSF73 degradation as it is for the yeast homolog Ysh1 (Lee et al., 2020), we treated the *UBE3D* KO cells with the proteasome-specific inhibitor MG132 and the ubiquitin-activating enzyme (E1) inhibitor TAK-243 (Hyer et al.,

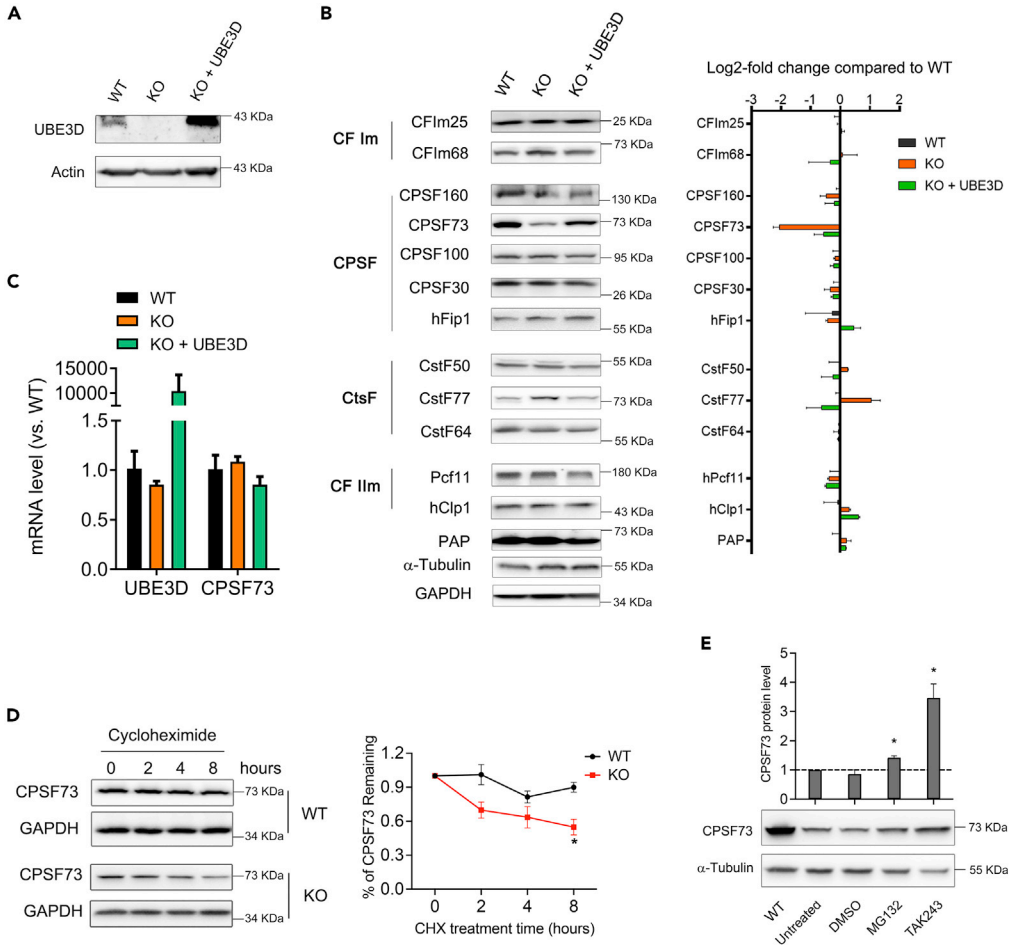

Figure 1. UBE3D positively regulates CPSF73 but not other C/P proteins at the post-translational level

(A) Western blot verification at the protein level of *UBE3D* KO in HEK293 cells and *UBE3D* addback to KO cells.

(B) CPSF73 was depleted in *UBE3D* KO cells and its level was restored by adding back UBE3D. Other C/P proteins were not depleted. A representative Western blot performed using antibodies specific to the subunits of the C/P complex is shown on the left panel. Quantitation of the log2-fold changes in protein levels compared to wild-type (WT) using two replicates is shown on the right.

(C) *CPSF73* mRNA level remained unchanged in *UBE3D*-negative and positive cells. Three biological replicates were analyzed by RT-qPCR, and values normalized to *RPL13A* expression.

(D) Cycloheximide (CHX) chase assay revealed that CPSF73 is less stable in *UBE3D* KO cells. Left panel, representative Western Blot and right panel, quantification of protein levels from three replicates, with values normalized to GAPDH.

(E) The level of CPFS73 in *UBE3D* KO cells was increased by the proteasome inhibitor MG132 (10 μM) and the E1 ubiquitin-activating enzyme inhibitor TAK243 (1 μM), demonstrating the degradation of CPFS73 was mediated by the ubiquitin-proteasome pathway. CPSF73 protein level with each treatment was normalized to the untreated control from two replicates. For all panels, error bars show the mean ± SEM; *p < 0.05; **p < 0.01; ***p < 0.001; ****p < 0.0001 (Student's *t* test, unpaired, two-tailed).

2018), followed by examining the levels of CPSF73. Western blot results (Figures 1E and S1D) showed that CPFS73 increased in *UBE3D* KO cells upon MG132 or TAK-243 treatment. Together, these results indicate that UBE3D stabilizes CPSF73 in human cells by preventing its ubiquitin-mediated proteasomal degradation.

UBE3D loss causes mRNA readthrough and global suppression of gene expression

Given that CPSF73 inactivation or depletion inhibits pre-mRNA cleavage and causes significant read-through transcription downstream of PASs and histone mRNA cleavage sites in metazoan cells (Eaton et al., 2018; Pettinati et al., 2018; Ross et al., 2020), we asked whether loss of UBE3D, which causes

CPSF73 down-regulation, would affect mRNA 3′ end processing and transcription termination. We used previously described primers to monitor cleavage of *ACTB* or *MYC* transcripts *in vivo* by RT-qPCR of total RNA reverse transcribed with random hexamers (Davidson et al., 2014; Eaton et al., 2018). These primer pairs detect unspliced transcripts (US) or RNA-containing sequence that spans the PAS (Span) (Figure 2A). When there is a cleavage defect at the PAS, more "Span" products are expected after normalization to "US" control. For both genes, the accumulation of RNA spanning the PAS indicated a significant reduction of PAS cleavage in *UBE3D* KO cells, with an increase of 2.9-fold for *ACTB* and 3.6-fold for *MYC*. When UBE3D expression was restored in KO cells, cleavage of both transcripts was rescued (Figure 2A).

To test the global effect of *UBE3D* depletion on transcription termination, we prepared RNA-seq libraries from WT and *UBE3D* KO cells and analyzed the data by DoGFinder (Wiesel et al., 2018), a software for the discovery and quantification of readthrough transcripts from RNA-seq. *UBE3D* KO caused 445 intergenic regions to exhibit an increase in the downstream of Gene-containing transcripts (DoGs) and 328 to show a decrease compared to WT (Figure 2B). We next asked if the changes in the level of DoGs were owing to changes in the expression levels of upstream genes. Correlation analysis showed that the majority of genes associated with an increase in DoGs generally did not show a corresponding increase in expression (Figure S2), indicating that the likely reason for DoG accumulation was the defect in 3′ end processing. Furthermore, many of the DoGs that are increased in KO cells are suppressed when UBE3D is added back (Figure 2C). The reads maps of representative genes are presented in Figure 2D. The reads downstream of histone gene *HIST2H2BC11* and non-histone gene *SNRPA* were strongly increased in *UBE3D* KO samples and decreased with *UBE3D* addback. These results show that, consistent with the concomitant CPSF73 degradation, *UBE3D* KO causes readthrough transcription at mRNA encoding genes.

As noted above, some DoGs showed decreased expression upon UBE3D loss. Many of the genes associated with decreased DoGs have a corresponding decrease in gene expression (Figure S2, lower left quadrant), an outcome that would be predicted if the transcription of these genes was decreased. Only 6 genes showed decreased DoGs with increased gene expression. Curiously, the majority of genes with decreased DoGs have no change in gene expression. Our analysis cannot discriminate the underlying reasons for these outcomes and whether they are direct or indirect consequences of *UBE3D* KO. Some genes may be poorly transcribed in the *UBE3D* KO cells, leading to the decrease in DoGs compared to *UBE3D* + cells, but the cell compensates by increasing the stability of the mRNAs of these genes so that the steady-state level remains the same.

Differential gene expression analysis of RNA-seq data in *UBE3D* KO samples showed that *UBE3D* KO led to a global downregulation of gene expression compared to WT (Figure 2E), and a global gene upregulation was observed when we expressed UBE3D protein in the KO cells (Figure 2F). The genes downregulated in KO cells shared a high overlap with genes upregulated by *UBE3D* addback (Figure 2G), indicating that UBE3D was responsible for the gene expression changes.

UBE3D depletion inhibits migration and invasion of breast cancer cells through down-regulating CPSF73

CPSF73 has been shown to correlate with different cancers and is considered a biomarker for prognosis as well as a target for cancer treatment (Liu and Moore, 2021). *CPSF73* knock-down reduced the migration of fibroblasts and triple-negative breast cancer cells (TNBC) (Mitra et al., 2018), a highly aggressive breast cancer subtype (Rakha and Ellis, 2009) in wound-healing assays *in vitro*. In addition, Kaplan Meier plots showed that a higher expression level of either UBE3D or CPSF73 correlates with a worse overall survival rate in patients with breast cancer (Figures S3A and S3B), indicating the clinical relevance of regulating UBE3D and CPSF73 levels. To test whether UBE3D also regulates CPSF73 in breast cancer cells, we tried to make *UBE3D* KO lines with the triple-negative breast cancer cell line MDA-MB-231 but could not recover cells with the knockout. Instead, we constructed two inducible *UBE3D* shRNA lines using MDA-MB-231 cells and a control cell line using shRNA targeting luciferase (sh.LUC). UBE3D immuno-staining showed a successful, doxycycline-inducible knockdown (KD) of UBE3D as well as a corresponding decrease in CPSF73 protein compared to the luciferase shRNA (Figure S3C). RT-qPCR showed that the *CPSF73* mRNA level in UBE3D KD samples was not significantly changed (Figure S3D), indicating that similar to HEK293 cells, the regulation of CPSF73 by UBE3D in triple-negative cancer cells is also at its protein level.

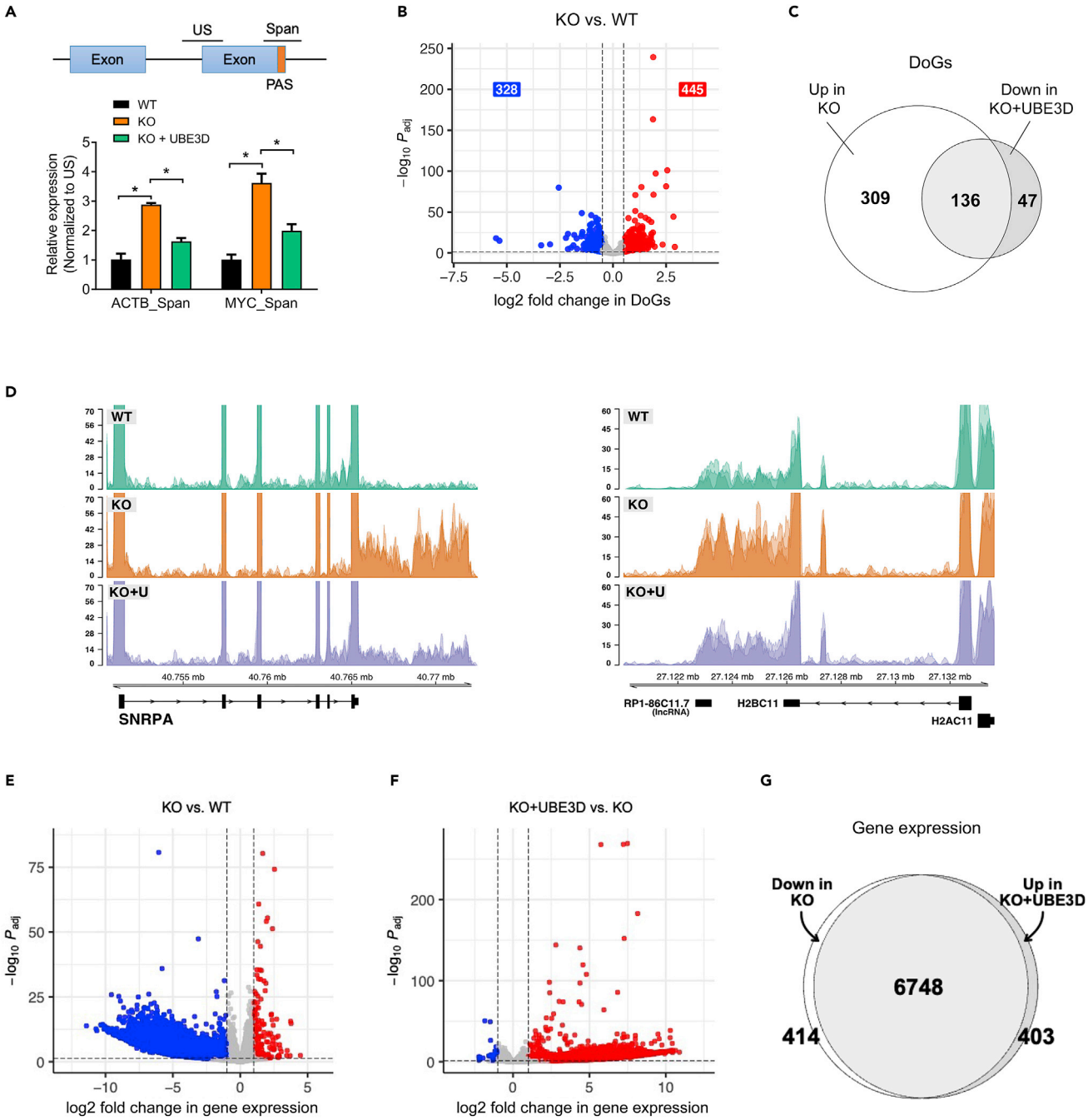

Figure 2. *UBE3D* KO leads to impaired 3′ end processing, transcriptional readthrough of PASs, and dysregulated gene expression

(A) Analysis of *ACTB* and *MYC* 3′ end processing in *UBE3D* WT and KO cells. The diagram depicts the relative positions of unspliced (US) and PAS spanning (Span) amplicons. Span values are expressed relative to *UBE3D* WT cells after normalizing to US RNA levels from each gene. Error bars show the mean ± SEM; *p < 0.05; **p < 0.01; ***p < 0.001; ****p < 0.0001 (Student's *t* test, unpaired, two-tailed) from two biological replicates

(B) Volcano plot of DoGs in *UBE3D* WT versus *UBE3D* KO cells showing the log2-fold change in DoG expression compared to the log10 P_{adj} value for each gene. A total of 2954 genes were identified with associated DoGs. Log_2 fold change cutoff, 0.5; P_{adj} −value cutoff, 0.05.

(C) Overlap analysis of DoGs upregulated in KO and DoGs downregulated in *UBE3D* addback samples.

(D) Reads maps of the non-histone mRNA *SNRPA* and histone mRNA *HIST2H2BC11* show increased transcriptional readthrough into intergenic regions after *UBE3D* KO and suppression of the DoGs after UBE3D expression in the KO cells (KO + U). Traces for the individual replicates are shown in different shades.

(E) Volcano plot of differential gene expression in *UBE3D* KO cell versus WT cells. Log_2 fold change cutoff, 1.0; P_{adj} −value cutoff, 0.05.

(F) Volcano plot of differential gene expression in UBE3D addback cells versus KO cells. Log_2 fold change cutoff, 1.0; P_{adj} −value cutoff, 0.05.

(G) Overlap analysis of genes downregulated in KO and genes upregulated in UBE3D addback samples. For all panels, error bars show the mean ± SEM; *p < 0.05; **p < 0.01; ***p < 0.001; ****p < 0.0001 (Student's *t* test, unpaired, two-tailed).

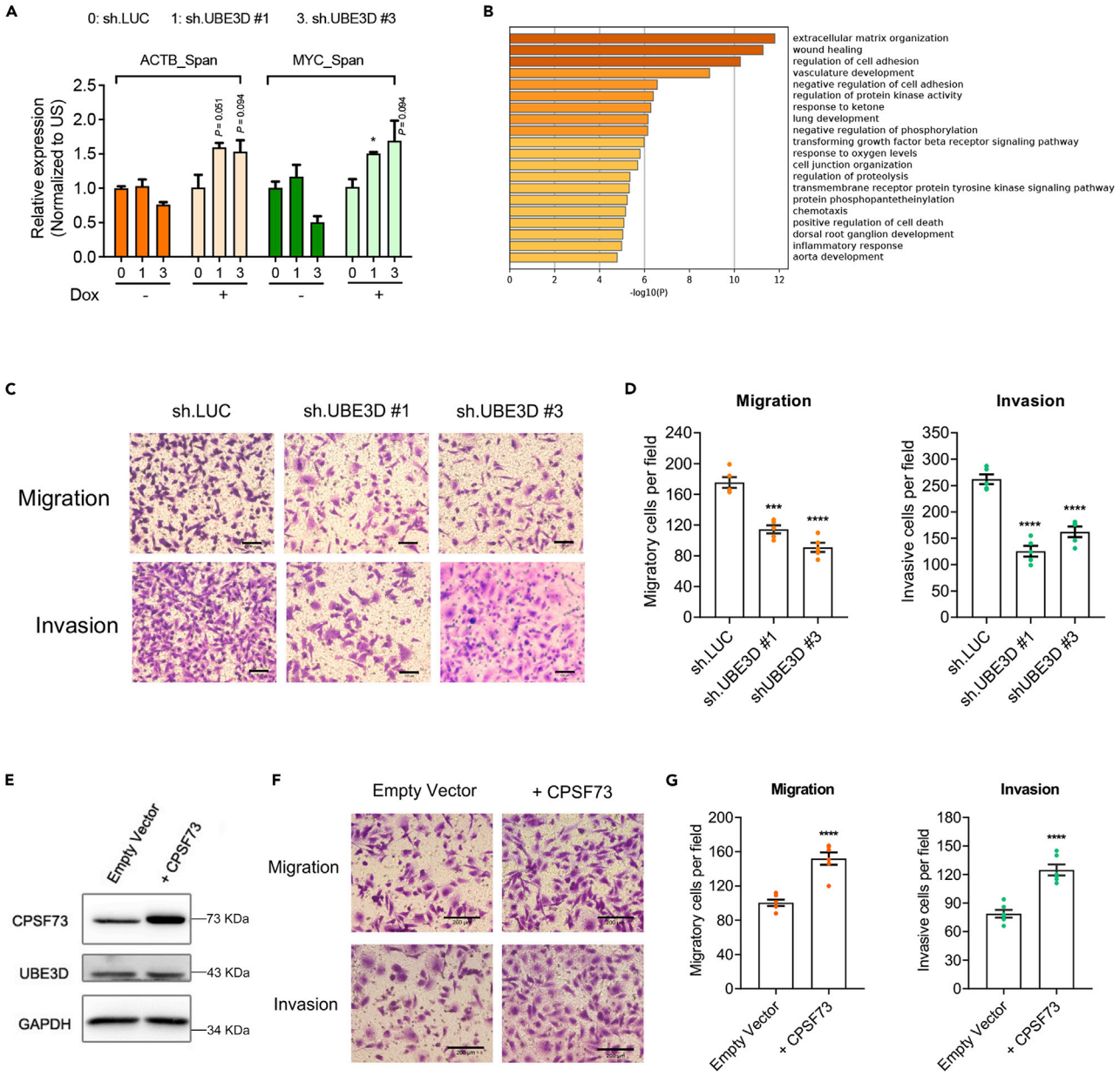

Figure 3. UBE3D depletion inhibits breast cancer cell motility in a CPFS73-dependent manner

(A) Analysis of mRNA 3′ end processing efficiency of *ACTB* and *MYC* transcripts in MDA-MB-231 after *UBE3D* KD from two biological replicates, as described in Figure 2A.

(B) GO term analysis of the genes downregulated in MDA-MB-231 *UBE3D* KD samples was performed using Metascape.

(C) Migration and invasion assessments in MDA-MB-231 cells upon UBE3D KD. Representative images of the migrated and invaded cells. Scale bar = 200 μm.

(D) Quantification of migratory and invasive cells upon UBE3D KD.

(E) CPSF73 overexpression in *UBE3D* KD cells was determined by Western blot.

(F and G) CPSF73 overexpression reversed the UBE3D KD-mediated MDA-MB-231 migration and invasion defects. Scale bar = 200 μm. For all panels, error bars show the mean ± SEM; *p < 0.05; **p < 0.01; ***p < 0.001; ****p < 0.0001 (Student's *t* test, unpaired, two-tailed).

Next, we tested the effect of downregulating UBE3D on mRNA 3′ end processing and transcription termination in breast cancer cells. RT-qPCR showed a 1.5-fold or greater increase in unprocessed *ACTB* and *MYC* transcripts in the *UBE3D* KD cells upon Dox induction compared to the sh.LUC control, and no increase in cells without Dox (Figure 3A), demonstrating that UBE3D loss caused a processing defect. *UBE3D* KD in MDA-MB-231 cells caused 280 genes to be downregulated and 113 genes to be upregulated

(Figure S3E). Gene ontology (GO) analysis of the 113 genes upregulated in *UBE3D* KD samples showed that the two most enriched terms were in the transmembrane receptor protein serine/threonine kinase signaling pathway (Figure S3F), while the GO terms of the 280 downregulated genes revealed that cell mobility related gene sets, including extracellular matrix organization, wound healing, regulation of cell adhesion, were the most significantly enriched (Figure 3B), suggesting that *UBE3D* KD might induce a defect in migration and invasion. Moreover, while wild-type MDA-MB-231 cells are spindle-shaped, the *UBE3D* KD cells show a more compact epithelial-like morphology (Figure S4A). Scratch wound healing and Transwell assays were used to determine how *UBE3D* affected cell motility. *UBE3D* KD inhibited MDA-MB-231 migration and slowed the closure of the scratch wound (Figure S4B). Similarly, *UBE3D* KD significantly reduced the migration of MDA-MB-231 cells in Transwell assays (Figures 3C and 3D). In addition, Transwell invasion assays showed that *UBE3D* KD also markedly impaired the ability of MDA-MB-231 cells to move through the extracellular matrix, a process critical for cancer metastasis (Figures 3C and 3D). Inhibition of migration and invasion was not a consequence of reduced proliferation, as *UBE3D* KD had no effect on cell growth (Figure S4C).

To determine if UBE3D promotes breast cancer cell mobility by maintaining CPSF73 function, we overexpressed CPSF73 by transient transfection for 24 h in *UBE3D* KD cells (Figure 3E) and performed Transwell assays. Compared to the empty vector control, CPSF73 overexpression rescued the breast cancer cell migration and invasion defects (Figures 3F and 3G), indicating that CPSF73 is the likely mediator of UBE3D function in breast cancer cells. Collectively, these results revealed that UBE3D and its interactor CPSF73 may play a key role in the progression of breast cancer via enhancing cell migration and invasion.

The CPSF73 inhibitor JTE-607 inhibits breast cancer cell migration, invasion, and self-renewal

The chemical JTE-607 was recently identified as a specific inhibitor of CPSF73 that acts by blocking RNA access to the nuclease's active site (Liu and Moore, 2021; Ross et al., 2020). It also inhibits the growth of acute myeloid leukemia (AML) and Ewing's sarcoma cancer, without a strong effect on most other types of cancer (Ross et al., 2020; Tajima et al., 2010; Uesato et al., 2006). As described above, the depletion of *CPSF73* slowed breast cancer migration, and we wanted to know whether catalytic inhibition of CPSF73 would also affect the motility of breast cancer cells. We determined that the IC50 of JTE-607 against MDA-MB-231 (Basal B type TNBC) or MDA-MB-468 (Basal A type TNBC) cells were both greater than 50 μM (Figures S5A and S6D). Consistent with CPSF73 as a target, JTE-607 at a 2.5 μM concentration inhibited the processing of both ACTB and MYC transcripts (Figure 4A and S6A). Interestingly, the spindle-like morphology of MDA-MB-231 was also changed with the JTE-607 treatment (Figure S5B) in a way similar to what we observed with *UBE3D* KD. Scratch wound healing (Figure S5C) and Transwell migration (Figures 4B and 4C) assays revealed the inhibition of migration, and the Transwell invasion assay showed a significant reduction of invasiveness (Figures 4B and 4C). In addition, similar results were observed in MDA-MB-468 cells with JTE-607 in Transwell migration and invasion assay (Figures S6B and S6C). Thus, catalytic inhibition of CPSF73 is sufficient to alter these breast cancer cell phenotypes.

Three-dimensional (3D) cultures of tumor cells such as MDA-MB-231 can more accurately recapitulate the *in vivo* microenvironment than 2D growth and are considered a better model to evaluate drug effectiveness, as cells grown in this way can be altered in their sensitivity to potential cancer drugs (Fang and Eglen, 2017; Gunness et al., 2013; Pinto et al., 2020). To further evaluate the inhibitory potential of JTE-607 in tumor progression, we treated cells with JTE-607 in 3D culture, in which cells are embedded in a 10% Matrigel. Branching structures formed by cancer cells in 3D culture are associated with tumor invasion and aggressive phenotypes (Kenny et al., 2007). JTE-607 significantly reduced the formation of these structures in MDA-MB-231 cells (Figure 4D). We only observed invasive branching in the MDA-MB-231 line, but not in the MDA-MB-468 cells (data not shown). To test the effectiveness of JTE-607 in inhibiting tumor cell proliferation in 3D cultures, we assayed the cell numbers by the CellTiter-Glo 3D Cell Viability Assay and calculated an IC_{50} value of 24.6 μM in MDA-MB-231 and an IC_{50} value of 15.1 μM in MDA-MB-468, respectively (Figures S5D and S6D), suggesting that basal TNBC cells in 3D cultures are sensitized to JTE-607 treatment. The formation of spheres when cancer cells are embedded in 50% Matrigel is an indication of the self-renewal ability of the cells, a defining property of cancer cell stemness that affects metastasis, drug resistance, and cancer recurrence (Bahmad et al., 2018). Both MDA-MB-231 and MDA-MB-468 cells treated with JTE-607 were defective in spheroid formation (Figures 4E and S6E). These results demonstrate that the catalytic inhibition of CPSF73 suppressed the invasive and self-renewal phenotypes of triple-negative breast cancer cells.

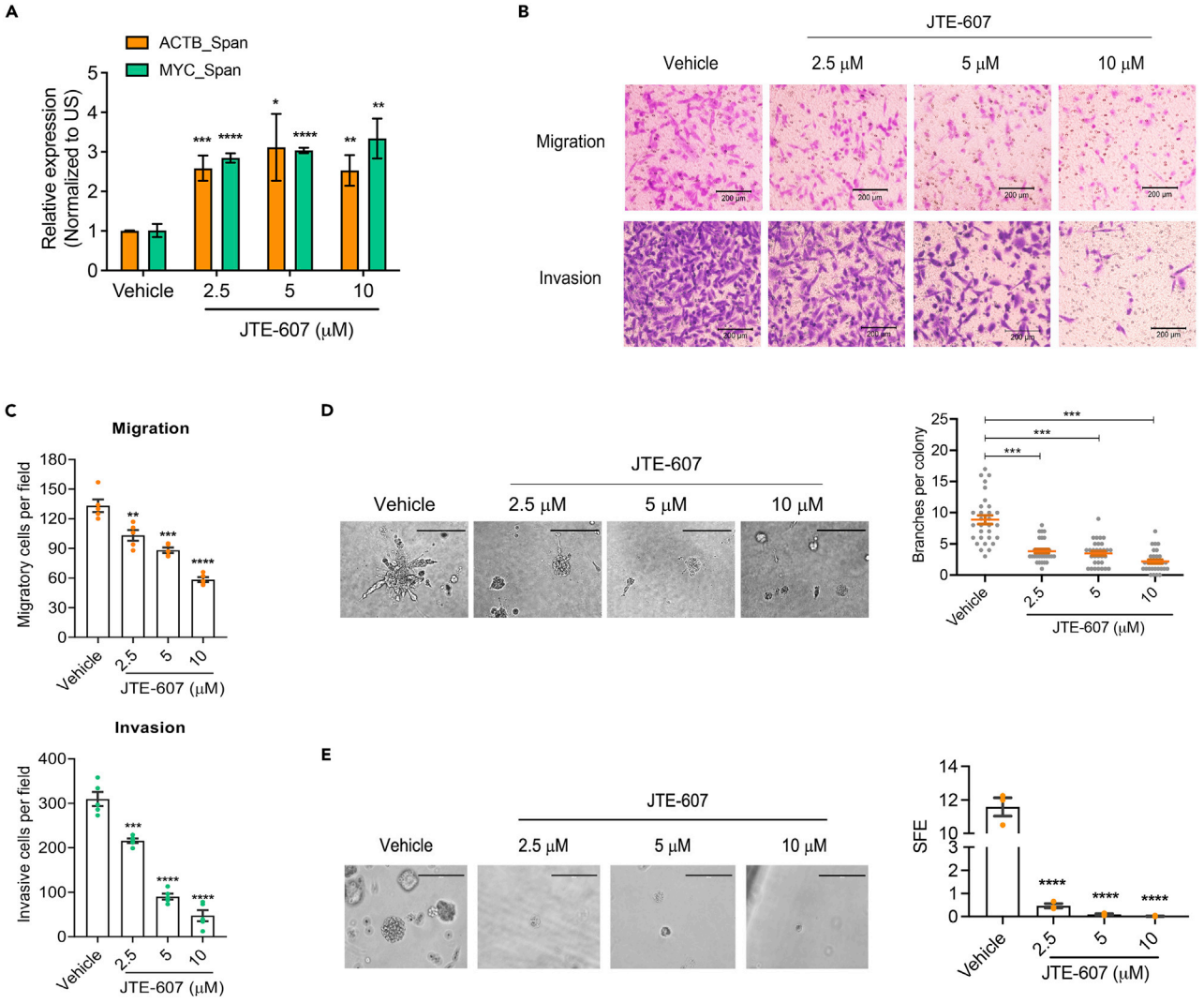

Figure 4. Catalytic inhibition of CPSF73 leads to breast cancer cell migration and invasion defects

(A) *ACTB* and *MYC* mRNA 3′ end processing in MDA-MB-231 cells treated with JTE-607, determined from three replicates.

(B and C) Transwell assays to evaluate the effects of JTE-607 treatment on cell migration and invasion. Representative images of the migrated and invaded cells (B) and quantitation data (C). Scale bar = 200 μm.

(D) JTE-607 reduced MDA-MB-231 cell branches in a 3D invasion assay. Right panel: quantification of branches from 30 to 50 colonies in each group.

(E) JTE-607 effectively inhibited MDA-MB-231 sphere formation in Matrigel. Spheres with a diameter over 50 μm were counted and quantified from three replicates. Representative images are shown. For all panels, error bars show the mean ± SEM; *p < 0.05; **p < 0.01; ***p < 0.001; ****p < 0.0001 (Student's *t* test, unpaired, two-tailed).

CPSF73 expression level correlates to breast cancer cell self-renewal properties

Given the essential roles of cancer stem cells in breast cancer oncogenesis and metastasis, next, we explored the impact of direct manipulation of *CPSF73* expression on breast cancer cell stemness. We made three inducible *CPSF73* KD MDA-MB-231 cell lines (Figure 5A) and assayed the self-renewal properties after Dox-inducible knockdown. Our results showed that directly reducing *CPSF73* mRNA levels inhibited breast cancer cell self-renewal, as determined by 3D sphere formation in Matrigel (Figures 5B and 5C). In contrast, when we overexpressed CPSF73 in MDA-MB-231 cells (Figure 5D), the self-renewal efficiency was enhanced, suggesting that *CPSF73* overexpression can drive the cancer cell self-renewal (Figures 5E and 5F). Neither knockdown nor overexpression of CPSF73 affected proliferation in 2D culture (Figure S7), indicating that these manipulations are mostly affecting the stem cell population. These findings are consistent with our results in MDA-MB-231 cells treated with JTE-607. Given the fact that self-renewal is an essential property of cancer stem cells, our results support the value of future studies on

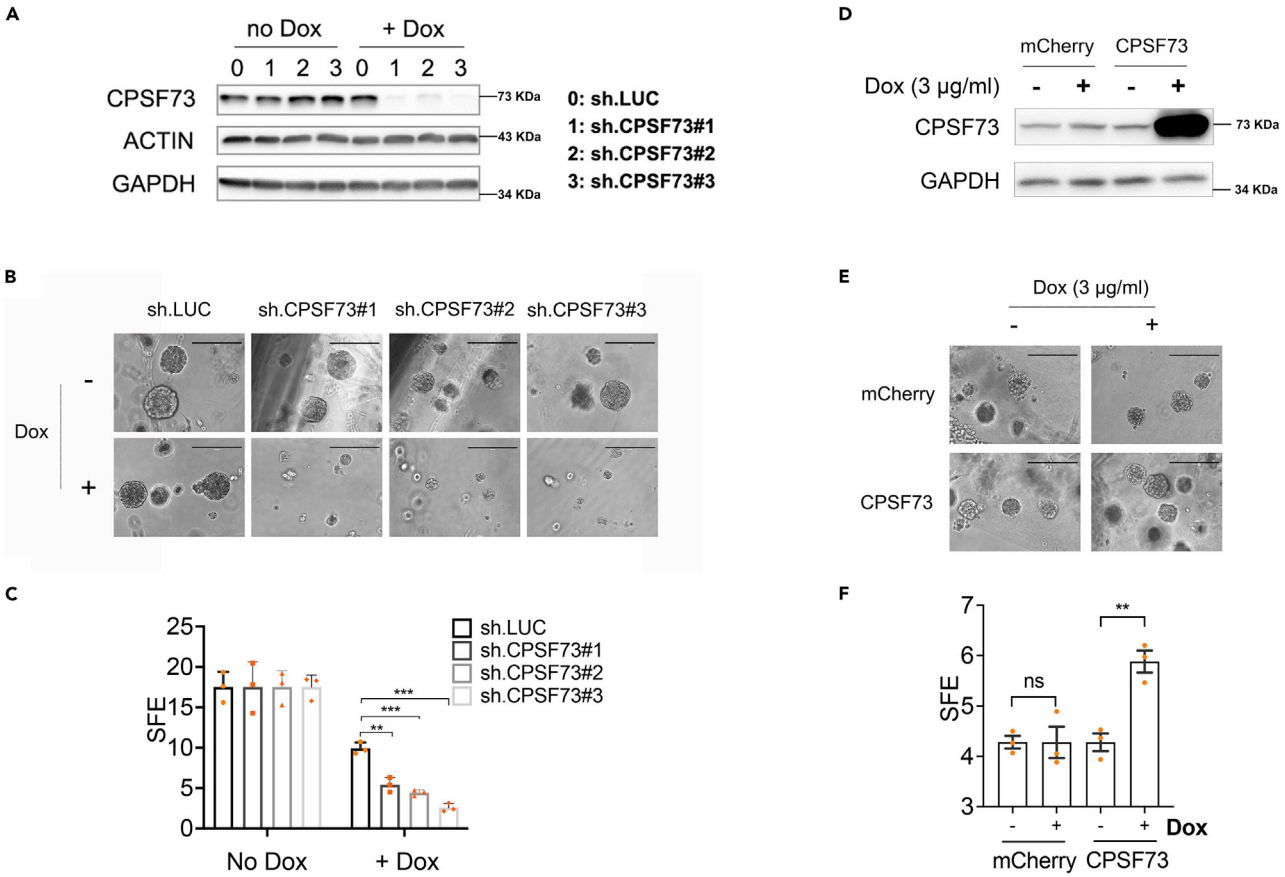

Figure 5. CPSF73 expression level correlates with breast cancer cell self-renewal properties

(A) CPSF73 knockdown by three independent inducible shRNAs in MDA-MB-231 cells.

(B and C) CPSF73 knockdown effectively inhibited MDA-MB-231 sphere formation in Matrigel. Spheres with a diameter over 50 μm were counted and quantified from three replicates. Representative images are shown. Scale bar = 200 μm.

(D) Doxycycline-inducible overexpression of CPSF73 in MDA-MB-231 cells. (E and F) CPSF73 overexpression (OE) promoted MDA-MB-231 sphere formation in Matrigel. Spheres with a diameter over 50 μm were counted and quantified from three replicates. Representative images are shown. Scale bar = 200 μm.

For all panels, error bars show the mean ± SEM; *p < 0.05; **p < 0.01; ***p < 0.001; ****p < 0.0001 (Student's *t* test, unpaired, two-tailed).

the potential of CPSF73 and other mRNA 3′end processing factors as targets to suppress stem cell self-renewal and reduce TNBC metastasis.

DISCUSSION

The essential endonuclease CPSF73, a protein highly conserved from archaea to single-cell and metazoan eukaryotes, plays a central role in the 3′ end processing of mRNA. UBE3D was reported as one of the CPSF73's interactors in human cells (Chen et al., 2014; Huttlin et al., 2017). In this study, we show that loss of UBE3D specifically decreases the level of CPSF73 but not that of other C/P proteins and this occurs at the post-translational level. We also demonstrated that targeting CPSF73 through *UBE3D* depletion or chemical inhibition disrupted mRNA 3′ end processing and transcription termination, and surprisingly, inhibited breast cancer cell migration, invasion, and tumor sphere formation, which are properties that contribute to metastasis and relapse. Moreover, decreasing the *CPSF73* mRNA level repressed sphere formation, while increasing the level enhanced it. Our findings support a previously unappreciated role for CPSF73 in promoting breast cancer cell stemness and suggest that understanding CPSF73's regulation may provide insights into new treatment avenues.

In our study, we found that CPSF73 downregulation on *UBE3D* depletion led to processing defects and increased gene readthrough transcripts. Poor 3′ end processing will negatively affect the mRNA output of the upstream gene, in agreement with our observation that many genes showed decreased expression

when CPSF73 was depleted. In addition to the direct consequences of poor 3′ end processing, CPSF73 dysfunction causes readthrough transcription as demonstrated here and in other studies (Eaton et al., 2018; Ross et al., 2020). Readthrough transcription can interfere with downstream gene transcription through promoter interference of genes arranged in tandem or alternatively, promote aberrant expression by generating RNA chimeras (Proudfoot, 2016). For convergent genes, it can trigger RNAi pathways or lead to RNA Polymerase II collisions (Proudfoot, 2016). Elongation into intergenic regions has been shown to remodel genome 3D organization and switch heterochromatin regions to chromatin permissive for transcription factor binding, and in this way, alter transcription programs (Heinz et al., 2018; Hennig et al., 2018). All of these consequences of poor processing and termination could contribute to the changes we have observed in cancer cell phenotypes when CPSF73 function is hindered.

The cell has found ways to naturally regulate CPSF73 activity at multiple levels—by recruiting it to different types of mRNA 3′ end processing complexes (reviewed in (Liu and Moore, 2021)), by limiting its association with the 3′ ends of transcribed genes, as has been observed after heat shock (Cardiello et al., 2018), by blocking its nuclear localization (Zhu et al., 2009), or by altering the level of its mRNA. Regarding the latter, the HIV-1 Tat protein increases *CPSF73* mRNA levels to regulate both viral and cellular gene expression (Calzado et al., 2004), and the eukaryotic translation initiation factor eIF4E promotes the processing and nuclear export of mRNAs of *CPSF73* and other CPSF subunits and consequently increases their protein levels (Davis et al., 2019). At the protein level, CPSF73 is subject to modification by SUMO and ubiquitin (Chen et al., 2014; Vethantham et al., 2007), but the consequences of such modifications have not been investigated except in yeast, where we showed that Ipa1 stabilizes Ysh1, the CPSF73 homolog, by inhibiting its ubiquitin-mediated proteasomal degradation (Lee et al., 2020). Our work with UBE3D, the Ipa1 counterpart, demonstrates that this regulatory mechanism is conserved.

Cancer cells frequently increase their transcriptional rate and the resulting stress on the pre-mRNA-processing machinery is a point that can be exploited therapeutically (Naro et al., 2021). The potential of this strategy is evident from a recent study showing that JTE-607, a specific CPSF73 inhibitor, suppressed the proliferation of specific types of cancer cells (Ross et al., 2020). JTE-607 was identified as an immunosuppressive agent over two decades ago and progressed to clinical studies with healthy human volunteers (Kakutani et al., 1999). In the study by Ross et al., profiling of cell viability across 92 cell lines of diverse lineages showed that AML and Ewing's sarcoma are the cell lines most sensitive to JTE-607 (Ross et al., 2020). Curiously, in comparison to these two cancers, the growth of the triple-negative cancer cell lines, MDA-MB-231 and MDA-MB-468, was relatively insensitive to JTE-607. However, we investigated the possibility that JTE-607 might have effects on cancer properties other than proliferation, such as metastasis and self-renewal. Indeed, we found that a low, non-cytotoxic dose of JTE-607 suppressed triple-negative breast cancer cell migration and invasion in both 2D and 3D cultures. These properties are indicative of a cancer cell's ability to metastasize, which is the main cause of death in patients with cancer. JTE-607 also repressed tumor sphere formation *in vitro*, which is a measurement of the percentage of cancer stem cells in a tumor cell population. These cells can self-renew as well as differentiate into the cells that form the bulk of a tumor and are responsible for tumor initiation, chemical, and radiation resistance, metastasis, and relapse, all of which are properties that lead to therapy failure and mortality (Desai et al., 2019; Du et al., 2019; Shibata and Hoque, 2019; Yang et al., 2020; Zhou et al., 2021). Depletion of *CPSF73* by shRNA-mediated knockdown or by interfering with *UBE3D* also supported the important role of CPSF73 in maintaining these cancer cell properties. In summary, our findings argue that the inhibition of pre-mRNA 3′ end processing, a fundamental cellular function, can be not only a druggable node for inhibiting cancer cell proliferation, but also for slowing cancer metastasis and recurrence.

Limitations of the study

This study described the conserved regulation of CPSF73 by UBE3D in human cells and revealed CPSF73 as a target for inhibiting triple-negative breast cancer migration, invasion, and self-renewal. In *UBE3D* KO cells, the increased DoGs can be interpreted by the depletion of CPSF73 while the decreased DoGs might be regulated by other pathways which are unclear. CPSF73 inhibition leads to gene readthrough, gene expression dysregulation, and alteration of triple-negative breast cancer cell properties. However, which mRNA expression changes or readthrough transcripts are mediating the output phenotypes have not been defined. Further work is necessary to comprehensively decode how an mRNA cleavage defect regulates breast cancer cell behavior. Additionally, whether targeting CPSF73 *in vivo* is sufficient to inhibit breast cancer growth and metastasis is unknown.

STAR★METHODS

Detailed methods are provided in the online version of this paper and include the following:

- KEY RESOURCES TABLE
- RESOURCE AVAILABILITY
  - Lead contact
  - Materials availability
  - Data and code availability
- EXPERIMENTAL MODEL AND SUBJECT DETAILS
  - Method details
  - Cycloheximide chase analysis
  - Treatment with ubiquitin and proteasome inhibitors
  - Gene readthrough analysis
  - Accession numbers
  - Transwell migration and invasion assays
  - 3D invasion assay
  - Sphere forming assay
  - Cell proliferation assay
  - Wound healing assay
  - Cell viability assay after JTE-607 treatment
- QUANTIFICATION AND STATISTICAL ANALYSIS

SUPPLEMENTAL INFORMATION

Supplemental information can be found online at https://doi.org/10.1016/j.isci.2022.104804.

ACKNOWLEDGMENTS

The authors acknowledge the Tufts University High-Performance Compute Cluster (https://it.tufts.edu/high-performance-computing) which was utilized for computational analyses reported in this article. We thank Rebecca E. Batorsky at Tufts Technology Services for help with RNA-seq data processing. We also thank all members of the Moore laboratory for discussions and comments on the article. This work was supported by the National Science Foundation grant MCB1244043 and the NIH grant R01 GM101010-01A1 to C. Moore.

AUTHOR CONTRIBUTIONS

H.L. and C.L.M. conceived the study. D.H. performed sequence data analysis. H.L. conducted laboratory experiments. H.L. and C.L.M. drafted and edited the article. All authors contributed to the interpretation of data and approved the final article. C.L.M. provided supervision and funding acquisition.

DECLARATION OF INTERESTS

The authors declare no competing interests.

Received: January 20, 2022
Revised: May 26, 2022
Accepted: July 15, 2022
Published: August 19, 2022

REFERENCES

Jafari Najaf Abadi, M.H., Shafabakhsh, R., Asemi, Z., Mirzaei, H.R., Sahebnasagh, R., Mirzaei, H., and Hamblin, M.R. (2019). CFIm25 and alternative polyadenylation: conflicting roles in cancer. Cancer. Lett. *459*, 112–121.

Bahmad, H.F., Cheaito, K., Chalhoub, R.M., Hadadeh, O., Monzer, A., Ballout, F., El-Hajj, A., Mukherji, D., Liu, Y.N., Daoud, G., and Abou-Kheir, W. (2018). Sphere-formation assay: three-dimensional in vitro culturing of prostate cancer stem/progenitor sphere-forming cells. Front. Oncol. *8*, 347.

Blighe, K., Rana, S., and Lewis, M. (2022). EnhancedVolcano: publication-ready volcano plots with enhanced colouring and labeling. https://bioconductor.org/packages/devel/bioc/vignettes/EnhancedVolcano/inst/doc/EnhancedVolcano.html.

Bonnal, S.C., López-Oreja, I., and Valcárcel, J. (2020). Roles and mechanisms of alternative splicing in cancer - implications for care. Nat. Rev. Clin. Oncol. *17*, 457–474.

Buels, R., Yao, E., Diesh, C.M., Hayes, R.D., Munoz-Torres, M., Helt, G., Goodstein, D.M., Elsik, C.G., Lewis, S.E., Stein, L., and Holmes, I.H. (2016). JBrowse: a dynamic web platform for genome visualization and analysis. Genome Biol. *17*, 66.

Calzado, M.A., Sancho, R., and Muñoz, E. (2004). Human immunodeficiency virus type 1 Tat increases the expression of cleavage and polyadenylation specificity factor 73-kilodalton subunit modulating cellular and viral expression. J. Virol. *78*, 6846–6854.

Cardiello, J.F., Goodrich, J.A., and Kugel, J.F. (2018). Heat shock causes a reversible increase in RNA polymerase II occupancy downstream of mRNA genes, consistent with a global loss in transcriptional termination. Mol. Cell. Biol. *38*, e00181-18.

Chen, C.Y., and Shyu, A.B. (2011). Mechanisms of deadenylation-dependent decay. Wiley Interdiscip. Rev. RNA *2*, 167–183.

Chen, S.L., Zhu, Z.X., Yang, X., Liu, L.L., He, Y.F., Yang, M.M., Guan, X.Y., Wang, X., and Yun, J.P. (2021). Cleavage and polyadenylation specific factor 1 promotes tumor progression via alternative polyadenylation and splicing in hepatocellular carcinoma. Front. Cell Dev. Biol. *9*, 616835.

Chen, T., Zhou, T., He, B., Yu, H., Guo, X., Song, X., and Sha, J. (2014). mUbiSiDa: a comprehensive database for protein ubiquitination sites in mammals. PLoS One *9*, e85744.

Costanzo, M., VanderSluis, B., Koch, E.N., Baryshnikova, A., Pons, C., Tan, G., Wang, W., Usaj, M., Hanchard, J., Lee, S.D., et al. (2016). A global genetic interaction network maps a wiring diagram of cellular function. Science *353*, aaf1420.

Davidson, L., Muniz, L., and West, S. (2014). 3 ' end formation of pre-mRNA and phosphorylation of Ser2 on the RNA polymerase II CTD are reciprocally coupled in human cells. Genes. Dev. *28*, 342–356.

Davis, M.R., Delaleau, M., and Borden, K.L.B. (2019). Nuclear eIF4E stimulates 3'-end cleavage of target RNAs. Cell Rep. *27*, 1397–1408.e4.

Desai, A., Yan, Y., and Gerson, S.L. (2019). Concise reviews: cancer stem cell targeted therapies: toward clinical success. Stem Cells Transl. Med. *8*, 75–81.

Desterro, J., Bak-Gordon, P., and Carmo-Fonseca, M. (2020). Targeting mRNA processing as an anticancer strategy. Nat. Rev. Drug. Discov. *19*, 112–129.

Dobin, A., Davis, C.A., Schlesinger, F., Drenkow, J., Zaleski, C., Jha, S., Batut, P., Chaisson, M., and Gingeras, T.R. (2013). STAR: ultrafast universal RNA-seq aligner. Bioinformatics *29*, 15–21.

Du, F.Y., Zhou, Q.F., Sun, W.J., and Chen, G.L. (2019). Targeting cancer stem cells in drug discovery: current state and future perspectives. World J. Stem Cells *11*, 398–420.

Eaton, J.D., Davidson, L., Bauer, D.L.V., Natsume, T., Kanemaki, M.T., and West, S. (2018). Xrn2 accelerates termination by RNA polymerase II, which is underpinned by CPSF73 activity. Genes Dev. *32*, 127–139.

Fang, Y., and Eglen, R.M. (2017). Three-dimensional cell cultures in drug discovery and development. SLAS Discov. *22*, 456–472.

Fellmann, C., Hoffmann, T., Sridhar, V., Hopfgartner, B., Muhar, M., Roth, M., Lai, D.Y., Barbosa, I.A.M., Kwon, J.S., Guan, Y., et al. (2013). An optimized microRNA backbone for effective single-copy RNAi. Cell Rep. *5*, 1704–1713.

Gruber, A.J., and Zavolan, M. (2019). Alternative cleavage and polyadenylation in health and disease. Nat. Rev. Genet. *20*, 599–614.

Gunness, P., Mueller, D., Shevchenko, V., Heinzle, E., Ingelman-Sundberg, M., and Noor, F. (2013). 3D organotypic cultures of human HepaRG cells: a tool for in vitro toxicity studies. Toxicol. Sci. *133*, 67–78.

Hein, M.Y., Hubner, N.C., Poser, I., Cox, J., Nagaraj, N., Toyoda, Y., Gak, I.A., Weisswange, I., Mansfeld, J., Buchholz, F., et al. (2015). A human interactome in three quantitative dimensions organized by stoichiometries and abundances. Cell *163*, 712–723.

Heinz, S., Texari, L., Hayes, M.G.B., Urbanowski, M., Chang, M.W., Givarkes, N., Rialdi, A., White, K.M., Albrecht, R.A., Pache, L., et al. (2018). Transcription elongation can affect genome 3D structure. Cell *174*, 1522–1536.e22.

Hennig, T., Michalski, M., Rutkowski, A.J., Djakovic, L., Whisnant, A.W., Friedl, M.S., Jha, B.A., Baptista, M.A.P., L'Hernault, A., Erhard, F., et al. (2018). HSV-1-induced disruption of transcription termination resembles a cellular stress response but selectively increases chromatin accessibility downstream of genes. PLoS Pathog. *14*, e1006954.

Hill, C.H., Boreikaitė, V., Kumar, A., Casañal, A., Kubík, P., Degliesposti, G., Maslen, S., Mariani, A., von Loeffelholz, O., Girbig, M., et al. (2019). Activation of the endonuclease that defines mRNA 3' ends requires incorporation into an 8-subunit core cleavage and polyadenylation factor complex. Mol. Cell. *73*, 1217–1231.e11.

Huang, L.Z., Li, Y.J., Xie, X.F., Zhang, J.J., Cheng, C.Y., Yamashiro, K., Chen, L.J., Ma, X.Y., Cheung, C.M.G., Wang, Y.S., et al. (2015). Whole-exome sequencing implicates UBE3D in age-related macular degeneration in East Asian populations. Nat. Commun. *6*, 6687.

Hundley, F.V., Sanvisens Delgado, N., Marin, H.C., Carr, K.L., Tian, R., and Toczyski, D.P. (2021). A comprehensive phenotypic CRISPR-Cas9 screen of the ubiquitin pathway uncovers roles of ubiquitin ligases in mitosis. Mol. Cell. *81*, 1319–1336.e9.

Huttlin, E.L., Bruckner, R.J., Paulo, J.A., Cannon, J.R., Ting, L., Baltier, K., Colby, G., Gebreab, F., Gygi, M.P., Parzen, H., et al. (2017). Architecture of the human interactome defines protein communities and disease networks. Nature *545*, 505–509.

Hyer, M.L., Milhollen, M.A., Ciavarri, J., Fleming, P., Traore, T., Sappal, D., Huck, J., Shi, J., Gavin, J., Brownell, J., et al. (2018). A small-molecule inhibitor of the ubiquitin activating enzyme for cancer treatment. Nat. Med. *24*, 186–193.

Kakutani, M., Takeuchi, K., Waga, I., Iwamura, H., and Wakitani, K. (1999). JTE-607, a novel inflammatory cytokine synthesis inhibitor without immunosuppression, protects from endotoxin shock in mice. Inflamm. Res. *48*, 461–468.

Kao, S.H., Wang, W.L., Chen, C.Y., Chang, Y.L., Wu, Y.Y., Wang, Y.T., Wang, S.P., Nesvizhskii, A.I., Chen, Y.J., Hong, T.M., and Yang, P.C. (2015). Analysis of protein stability by the cycloheximide chase assay. Bio. Protoc. *5*, e1374.

Kenny, P.A., Lee, G.Y., Myers, C.A., Neve, R.M., Semeiks, J.R., Spellman, P.T., Lorenz, K., Lee, E.H., Barcellos-Hoff, M.H., Petersen, O.W., et al. (2007). The morphologies of breast cancer cell lines in three-dimensional assays correlate with their profiles of gene expression. Mol. Oncol. *1*, 84–96.

Kobirumaki, F., Miyauchi, Y., Fukami, K., and Tanaka, H. (2005). A novel UbcH10-binding protein facilitates the ubiquitinylation of cyclin B in vitro. J. Biochem. *137*, 133–139.

Komini, C., Theohari, I., Lambrianidou, A., Nakopoulou, L., and Trangas, T. (2021). PAPOLA contributes to cyclin D1 mRNA alternative polyadenylation and promotes breast cancer cell proliferation. J. Cell. Sci. *134*, jcs252304.

Larsson, J. (2020). Eulerr: Area-Proportional Euler and Venn Diagrams with Ellipses. R Package Version 610.

Lee, S.D., Liu, H.Y., Graber, J.H., Heller-Trulli, D., Kaczmarek Michaels, K., Cerezo, J.F., and Moore, C.L. (2020). Regulation of the Ysh1 endonuclease of the mRNA cleavage/polyadenylation complex by ubiquitin-mediated degradation. RNA Biol. *17*, 689–702.

Lin, A., Ji, P., Niu, X., Zhao, X., Chen, Y., Liu, W., Liu, Y., Fan, W., Sun, Y., Miao, C., et al. (2021). CstF64-induced shortening of the BID 3'UTR promotes esophageal squamous cell carcinoma progression by disrupting ceRNA crosstalk with ZFP36L2. Cancer. Res. *81*, 5638–5651.

Liu, H., and Moore, C.L. (2021). On the cutting edge: regulation and therapeutic potential of the mRNA 3' end nuclease. Trends. Biochem. Sci. *46*, 772–784.

Love, M.I., Huber, W., and Anders, S. (2014). Moderated estimation of fold change and dispersion for RNA-seq data with DESeq2. Genome. Biol. *15*, 550.

Luo, K., Geng, J., Zhang, Q., Xu, Y., Zhou, X., Huang, Z., Shi, K.Q., Pan, C., and Wu, J. (2019). LncRNA CASC9 interacts with CPSF3 to regulate TGF- signaling in colorectal cancer. J. Exp. Clin. Cancer. Res. *38*, 249.

Martin, M. (2011). Cutadapt removes adapter sequences from high-throughput sequencing reads. EMBnet. J. *17*, 10–12.

Mitra, M., Johnson, E.L., Swamy, V.S., Nersesian, L.E., Corney, D.C., Robinson, D.G., Taylor, D.G., Ambrus, A.M., Jelinek, D., Wang, W., et al. (2018). Alternative polyadenylation factors link cell cycle to migration. Genome. Biol. *19*, 176.

Moore, K.S., and von Lindern, M. (2018). RNA binding proteins and regulation of mRNA translation in erythropoiesis. Front. Physiol. *9*, 910.

Naro, C., Bielli, P., and Sette, C. (2021). Oncogenic dysregulation of pre-mRNA processing by protein kinases: challenges and therapeutic opportunities. FEBS J. *288*, 6250–6272.

Ning, Y., Liu, W., Guan, X., Xie, X., and Zhang, Y. (2019). CPSF3 is a promising prognostic biomarker and predicts recurrence of non-small cell lung cancer. Oncol. Lett. *18*, 2835–2844.

Offenbacher, S., Divaris, K., Barros, S.P., Moss, K.L., Marchesan, J.T., Morelli, T., Zhang, S., Kim, S., Sun, L., Beck, J.D., et al. (2016). Genome-wide association study of biologically informed periodontal complex traits offers novel insights into the genetic basis of periodontal disease. Hum. Mol. Genet. *25*, 2113–2129.

Pearson, E.L., Graber, J.H., Lee, S.D., Naggert, K.S., and Moore, C.L. (2019). Ipa1 is an RNA polymerase II elongation factor that facilitates termination by maintaining levels of the poly(A) site endonuclease Ysh1. Cell Rep. *26*, 1919–1933.e5.

Pettinati, I., Grzechnik, P., Ribeiro de Almeida, C., Brem, J., McDonough, M.A., Dhir, S., Proudfoot, N.J., and Schofield, C.J. (2018). Biosynthesis of histone messenger RNA employs a specific 3′ end endonuclease. Elife *7*, e39865.

Pinto, B., Henriques, A.C., Silva, P.M.A., and Bousbaa, H. (2020). Three-dimensional spheroids as in vitro preclinical models for cancer research. Pharmaceutics *12*, 1186.

Proudfoot, N.J. (2016). Transcriptional termination in mammals: stopping the RNA polymerase II juggernaut. Science *352*, aad9926.

Rakha, E.A., and Ellis, I.O. (2009). Triple-negative/basal-like breast cancer: review. Pathology *41*, 40–47.

Ran, F.A., Hsu, P.D., Wright, J., Agarwala, V., Scott, D.A., and Zhang, F. (2013). Genome engineering using the CRISPR-Cas9 system. Nat. Protoc. *8*, 2281–2308.

Ren, F., Zhang, N., Zhang, L., Miller, E., and Pu, J.J. (2020). Alternative Polyadenylation: a new Frontier in post transcriptional regulation. Biomark. Res. *8*, 67.

Ross, N.T., Lohmann, F., Carbonneau, S., Fazal, A., Weihofen, W.A., Gleim, S., Salcius, M., Sigoillot, F., Henault, M., Carl, S.H., et al. (2020). CPSF3-dependent pre-mRNA processing as a druggable node in AML and Ewing's sarcoma (vol 13, pg 465, 2019). Nat. Chem. Biol. *16*, 479.

Rovadoscki, G.A., Pertile, S.F.N., Alvarenga, A.B., Cesar, A.S.M., Pértille, F., Petrini, J., Franzo, V., Soares, W.V.B., Morota, G., Spangler, M.L., et al. (2018). Estimates of genomic heritability and genome-wide association study for fatty acids profile in Santa Ines sheep. BMC. Genom. *19*, 375.

Shibata, M., and Hoque, M.O. (2019). Targeting cancer stem cells: a strategy for effective eradication of cancer. Cancers *11*, 732.

Stephens, M. (2017). False discovery rates: a new deal. Biostatistics *18*, 275–294.

Stewart, M. (2019). Polyadenylation and nuclear export of mRNAs. J. Biol. Chem. *294*, 2977–2987.

Sun, Y., Hamilton, K., and Tong, L. (2020). Recent molecular insights into canonical pre-mRNA 3 ′-end processing. Transcription *11*, 83–96.

Tajima, N., Fukui, K., Uesato, N., Maruhashi, J., Yoshida, T., Watanabe, Y., and Tojo, A. (2010). JTE-607, a multiple cytokine production inhibitor, induces apoptosis accompanied by an increase in p21(waf1/cip1) in acute myelogenous leukemia cells. Cancer Sci. *101*, 774–781.

Uesato, N., Fukui, K., Maruhashi, J., Tojo, A., and Tajima, N. (2006). JTE-607, a multiple cytokine production inhibitor, ameliorates disease in a SCID mouse xenograft acute myeloid leukemia model. Exp. Hematol. *34*, 1385–1392.

Vethantham, V., Rao, N., and Manley, J.L. (2007). Sumoylation modulates the assembly and activity of the pre-mRNA 3′ processing complex. Mol. Cell. Biol. *27*, 8848–8858.

Vichai, V., and Kirtikara, K. (2006). Sulforhodamine B colorimetric assay for cytotoxicity screening. Nat. Protoc. *1*, 1112–1116.

Gómez-Rubio, V. (2017). ggplot2-elegant graphics for data analysis. J. Stat. Software *77*, 1–3.

Wiesel, Y., Sabath, N., and Shalgi, R. (2018). DoGFinder: a software for the discovery and quantification of readthrough transcripts from RNA-seq. BMC. Genom. *19*, 597.

Xia, H., Zhang, Q., Shen, Y., Bai, Y., Ma, X., Zhang, B., Qi, Y., Zhang, J., Hu, Q., Du, W., et al. (2020). ube3d, a new gene associated with age-related macular degeneration, induces functional changes in both in vivo and in vitro studies. Mol. Ther. Nucleic Acids *20*, 217–230.

Yang, L., Shi, P., Zhao, G., Xu, J., Peng, W., Zhang, J., Zhang, G., Wang, X., Dong, Z., Chen, F., and Cui, H. (2020). Targeting cancer stem cell pathways for cancer therapy. Signal Transduct. Targeted Ther. *5*, 8.

Zhang, Y., Sun, Y., Shi, Y., Walz, T., and Tong, L. (2020). Structural insights into the human pre-mRNA 3 ′-End processing machinery. Mol. Cell. *77*, 800–809.e6.

Zhou, H.M., Zhang, J.G., Zhang, X., and Li, Q. (2021). Targeting cancer stem cells for reversing therapy resistance: mechanism, signaling, and prospective agents. Signal Transduct. Targeted Ther. *6*, 62.

Zhou, Y., Zhou, B., Pache, L., Chang, M., Khodabakhshi, A.H., Tanaseichuk, O., Benner, C., and Chanda, S.K. (2019). Metascape provides a biologist-oriented resource for the analysis of systems-level datasets. Nat. Commun. *10*, 1523.

Zhu, Z.H., Yu, Y.P., Shi, Y.K., Nelson, J.B., and Luo, J.H. (2009). CSR1 induces cell death through inactivation of CPSF3. Oncogene *28*, 41–51.

STAR★METHODS

KEY RESOURCES TABLE

REAGENT or RESOURCE	SOURCE	IDENTIFIER
Antibodies		
Rabbit polyclonal anti-UBE3D	Abnova	Cat#PAB21883; RRID: AB_10966255
Rat monoclonal α-Tubulin Antibody	Thermo Fisher Scientific	Cat#MA1-80189; RRID: AB_2210200
Mouse monoclonal anti-GAPDH antibody (G-9)	Santa Cruz Biotechnology	Cat#sc-365062; RRID: AB_10847862
Rabbit polyclonal anti-CPSF160	Bethyl	Cat#A301-580A; RRID: AB_1078859
Rabbit polyclonal anti-CPSF100	Bethyl	Cat#A301-581A; RRID: AB_1078861
Mouse monoclonal anti-CPSF73 antibody (C-3)	Santa Cruz Biotechnology	Cat#sc-393001
Mouse monoclonal anti-CPSF4 antibody (D-1)	Santa Cruz Biotechnology	Cat#sc-390516
Mouse monoclonal anti-FIP1L1 antibody (C-10)	Santa Cruz Biotechnology	Cat#sc-398392; RRID: AB_2811203
Mouse monoclonal anti-Symplekin antibody (G-6)	Santa Cruz Biotechnology	Cat#sc-398897; RRID: AB_2811202
Mouse monoclonal anti-WDR33 antibody (D-1)	Santa Cruz Biotechnology	Cat#sc-374466; RRID: AB_10988720
Mouse monoclonal anti-CstF64		C. MACDONALD
Mouse monoclonal anti-CstF77 antibody (G-5)	Santa Cruz Biotechnology	Cat#sc-376575; RRID: AB_11151026
Rabbit polyclonal anti-CstF50	Bethyl	Cat#A301-250A; RRID: AB_890586
Mouse monoclonal anti-NUDT21 antibody (2203C3)	Santa Cruz Biotechnology	Cat#sc-81109; RRID: AB_2153989
Rabbit polyclonal anti-CFIm68	Bethyl	Cat#A301-358A; RRID: AB_937785
Mouse monoclonal anti-Pcf11 antibody (A-7)	Santa Cruz Biotechnology	Cat#sc-515669
Rabbit polyclonal anti-hClp1	Invitrogen	Cat#AAS02642C
Rabbit polyclonal anti-PAP antibody (H-300)	Santa Cruz Biotechnology	Cat#sc-32915; RRID: AB_2159213
Chemicals, peptides, and recombinant proteins		
Polybrene	EMD Millipore	Cat#TR-1003-G
Puromycin	InvivoGen	Cat#ant-pr-1
Doxycycline	Fisher Scientific	Cat#10592-13-9
Cycloheximide	EMD Millipore	Cat#AC357420010
MG-132	Sigma-Aldrich	Cat#474790-5MG
TAK-243	MedChem Express	Cat#HY-100487
Chloroquine Diphosphate	Fisher Scientific	Cat#AAJ6445914
JTE-607	Tocris	Cat#5185
Sulforhodamine B	Fisher Scientific	Cat#3520-42-1
Crystal Violet	Thermo Scientific	Cat#548-62-9
BSA solution	Sigma-Aldrich	Cat#9048-46-8
EGF	R&D Systems	Cat#236-EG-200
FGF	R&D Systems	Cat#233-FB-025
B-27	Life Technologies	Cat#17504044
Matrigel	VWR	Cat#47743-718
Fugene	Promega	Cat#E2311
Critical commercial assays		
SURVEYOR assay	Transgenomic	Cat#706025
Monarch® Total RNA Miniprep Kit	New England BioLabs	Cat#T2010S
LunaScript® RT Super-Mix Kit	New England BioLabs	Cat#E3010S
Luna® Universal qPCR Master Mix Kit	New England BioLabs	Cat#M3003L
CellTiter-Glo Luminescent Cell Viability Assay	Promega	Cat#G7572

(*Continued on next page*)

Continued

REAGENT or RESOURCE	SOURCE	IDENTIFIER
Deposited data		
HEK293 UBE3D KO RNA-seq	This paper	GEO GSE189746
MDA-MB-231 UBE3D KD RNA-seq	This paper	GEO GSE189723
Experimental models: Cell lines		
HEK-293	ATCC	CRL-1573
HEK-293_UBE3D_KO	This paper	N/A
MDA-MB-231	ATCC	CRM-HTB-26
MDA-MB-231_UBE3D KD#1	This paper	N/A
MDA-MB-231_UBE3D KD#2	This paper	N/A
MDA-MB-231_UBE3D KD#3	This paper	N/A
MDA-MB-231_CPSF73 KD#1	This paper	N/A
MDA-MB-231_CPSF73 KD#2	This paper	N/A
MDA-MB-231_CPSF73 KD#3	This paper	N/A
MDA-MB-231_mCherry OE	This paper	N/A
MDA-MB-231_CPSF73 OE	This paper	N/A
MDA-MB-468	ATCC	HTB-132
Oligonucleotides		
sgRNAs for UBE3D KO	This paper (Table S1)	N/A
shRNAs for inducible UBE3D KD	This paper (Table S1)	N/A
shRNAs for inducible CPSF73 KD	This paper (Table S1)	N/A
Primers for SURVEYOR assay	This paper (Table S1)	N/A
CPSF73 qPCR primers	This paper (Table S1)	N/A
UBE3D qPCR primers	This paper (Table S1)	N/A
ACTB US primers	This paper (Table S1)	N/A
ACTB Span primers	This paper (Table S1)	N/A
MYC US primers	This paper (Table S1)	N/A
MYC Span primers	This paper (Table S1)	N/A
Recombinant DNA		
Constitutive human shUBE3D#1	Sigma-Aldrich	Cat#TRCN0000146557
Constitutive human shUBE3D#2	Sigma-Aldrich	Cat#TRCN0000146775
Constitutive scramble shRNA control	Addgene	Plasmis#1864
Inducible human shUBE3D#1	This paper	N/A
Inducible human shUBE3D#3	This paper	N/A
Inducible shLUC (LT3GEPIR)	Addgene	Plasmid#111177
UBE3D Human Tagged ORF Clone	ORIGENE	Cat#RC210924
CPSF73 Human Tagged ORF Clone	ORIGENE	Cat#RC205834
pSpCas9(BB)-2A-GFP	Addgene	Plasmid#48138
pSpCas9(BB)-2A-GFP-UBE3D #3	This paper	N/A
Inducible human shCPSF73#1	This paper	N/A
Inducible human shCPSF73#2	This paper	N/A
Inducible human shCPSF73#3	This paper	N/A
pSBtet-mCherry	This paper	N/A
pSBtet-CPSF73	This paper	N/A

(*Continued on next page*)

Continued

REAGENT or RESOURCE	SOURCE	IDENTIFIER
Software and algorithms		
GraphPad Prism v8	GraphPad software	https://www.graphpad.com/
ImageJ	ImageJ	https://imagej.net/Fiji
Cutadapt	Martin (2011)	https://cutadapt.readthedocs.io/en/stable/
STAR	Dobin et al. (2013)	https://github.com/alexdobin/STA
DESeq2	Love et al. (2014)	https://bioconductor.org/packages/release/bioc/html/DESeq2.html
custom code	This paper	N/A

RESOURCE AVAILABILITY

Lead contact

Further information and requests for resources and reagents should be directed to and will be fulfilled by the lead contact, Claire L. Moore (claire.moore@tufts.edu).

Materials availability

- Plasmids generated in this study will be made available upon request to the lead contact.
- Edited HEK293 cells and MDA-MB-231 cells generated in this study will be made available upon request to the lead contact.

Data and code availability

- All datasets generated or analyzed during this study are included in the published article. Detailed datasets supporting the current study are available from the lead contact upon request.
- RNA-seq data have been deposited at GEO and are publicly available as of the date of publication. Accession numbers are listed in the key resources table.
- This paper does not report original code. Custom code is available from the lead contact upon request.
- Any additional information required to reanalyze the data reported in this paper is available from the lead contact upon request.

EXPERIMENTAL MODEL AND SUBJECT DETAILS

Cell lines and cell culture The human embryonic kidney HEK293 and triple-negative breast cancer MDA-MB-231 and MDA-MB-468 cell lines used in this study were cultured in Dulbecco's modified Eagle medium (DMEM) with 10% fetal bovine serum (FBS) and 1% penicillin/streptomycin (10,000 U/mL). HEK293FT cells were grown in Dulbecco's modified Eagle medium (DMEM) with 10% FBS, 1 mM sodium pyruvate, 2 mM L-glutamine, 1 mM MEM Non-Essential Amino Acids and 1% penicillin/streptomycin. All cells were grown at 37 °C with 5% CO_2.

Plasmids, viral infection, overexpression and stable cell line generation The LT3GEPIR vector (Fellmann et al., 2013) used for constructing inducible shRNAs was purchased from Addgene. Human shRNAs against *UBE3D* (shUBE3D#1, ATTCAATCACCAAACTGTCTGA; shUBE3D#2, TTTTATTATGACTTCACCGCAG; shUBE3D#3, TTTGATTAAACATTGAAATCAG) or *CPSF73* (shCPSF73#1, TTGAATTTCTAATTCTTCCACA; shCPSF73#2, TAATATTAGGAATTTCAGCTGC; shCPSF73#3, TAATACATGATCTTCCTACTTC) were integrated into LT3GEPIR vector for inducible expression. shUBE3D#2 did not work for knockdown (data not shown). The small hairpin RNA sequence targeting luciferase was used as control (Fellmann et al., 2013). To generate lentiviruses, HEK293FT cells were co-transfected with the viral plasmid of interest and packaging and envelope plasmids using Fugene (Promega, E2311). Virus-containing supernatants were collected at 48 h after transfection. Target cells were infected with 0.45 μM-filtered viral supernatants in the culture medium supplemented with 8 μg/mL polybrene for 24 h. After 24 h, virus-containing medium was removed, and cells were grown in serum-containing medium for 24 h. Lentivirus-infected MDA-MB-231 cells were continuously selected by puromycin (2 μg/mL). For inducing shRNA expression, doxycycline

was added into the medium at final concentration of 1.5 μg/mL and cells were monitored by fluorescence microscope for GFP expression. The knockdown of target protein was confirmed by immunoblot and RT-qPCR analysis.

For overexpression, plasmids encoding the open reading frames of *UBE3D* (NM_198920.3) and *CPSF73* (NM_016207.4) were purchased from Genscript. pSBtet-GP was a gift from Eric Kowarz (Addgene plasmid # 60,495). Human *CPSF73* (NM_016207.4) were subcloned into pSBtet-GP following the strategy described by Kowarz et al.19 to produce pSBtet-CPSF73. pCMV(CAT)T7-SB100 was used as a helper vector to supply the Sleeping Beauty transposase. pCMV(CAT)T7-SB100 was a gift from Zsuzsanna Izsvak (Addgene plasmid # 34,879). Each pSBtet plasmid was mixed 9:1 with helper plasmid in Opti-MEM (Gibco, 31,985,062). Transfection was performed using Lipofectamine 3000 (Invitrogen, L3000001) according to the manufacturer's instructions. Cells which had successfully integrated the Sleeping Beauty cassette were selected using puromycin (2 μg/mL). Successful selection was confirmed by monitoring the percentage of GFP-positive cells. To induce overexpression, cells were cultured in fresh growth media with 1.5 μg/mL doxycycline.

Method details

*CRISPR/Cas9 knockout*Knocking out (KO) of *UBE3D* in HEK293 cells was performed using the CRISPR/Cas9 genome editing system as previous described (Ran et al., 2013). The guide RNA sequence (AAAGGAA TTCACACGGCGAAGGG) against human *UBE3D* was designed using CHOPCHOP software (http://chopchop.cbu.uib.no/) and cloned into pSpCas9(BB)-2A-GFP (Addgene plasmid ID: 48,138). HEK293 cells were transfected using Fugene, and GFP-positive cells were sorted by FACS and isolated into single cell clones of *UBE3D* knockout cells. The knockout efficiency was confirmed by SURVEYOR assay as reported (Ran et al., 2013) and immunoblot analysis.

*Gene expression analysis by RT-qPCR*The extraction and purification of total RNA was performed using Monarch Total RNA Miniprep Kit (New England BioLabs, T2010S) according to the manufacturer's protocol. RNA concentration and quality was determined using the NanoDrop 2000 spectrophotometer before downstream processing. Reverse transcription of isolated RNA was performed using the LunaScript RT Super-Mix Kit (New England BioLabs, E3010S) according to the manufacturer's instructions. qPCR was performed on a CFX96 Touch Real-Time PCR Detection System in 96-well plates with the primers listed in Table S1 cDNA was added to the Luna Universal qPCR Master Mix Kit (New England BioLabs, M3003L) in a total reaction volume of 10 μL, and qPCR carried out according to the manufacturer's instructions. Target gene expression was normalized to that of human *RPL13A*. Comparative 2DDCt methods were used for the quantification of qPCR results.

*Western blotting*Protein was extracted from whole cells by lysis in RIPA buffer (Thermo Fisher Scientific, 89,900) supplemented with Halt Protease Inhibitor Cocktail (Thermo Fisher Scientific, 87,786). Cells were lysed on ice for 10 min and then homogenized by vortexing. Lysates were cleared by centrifugation at 12,000 x g for 15 min at 4 °C. Supernatants were collected and total protein content quantified by BCA assay (Thermo Fisher Scientific, 23,227). Lysates were normalized by total protein content and prepared for western blotting with the addition of 4X SDS Sample Buffer (+355 mM β-mercaptoethanol) and heated to 95 °C for 10 min. Lysates (20-80 mg) were resolved on 10% SDS gels and transferred to PVDF membranes. Total protein staining was performed using Revert Total Protein Stain (LI-COR, 926-11021). Membranes were blocked for 5 min using EveryBlot Blocking Buffer (Bio-Rad, 12,010,020). All primary antibodies were diluted in EveryBlot Blocking Buffer and incubated with membrane overnight at 4 °C. Membranes were washed three times in TBS +1% TWEEN 20 and incubated with HRP (HorseRadish Peroxidase) labeled secondary antibodies (1:10,000) for 1h at room temperature. Chemiluminescence signal was captured using the Syngene Imager and the band intensity was quantified using ImageJ.

Cycloheximide chase analysis

UBE3D KO cells were seeded at a density of 5×10^5 cells per well in a 6-well plate and grown in DMEM medium. On the day of the experiment, the medium was replaced with fresh DMEM medium containing 100 μg/mL cycloheximide and incubated for the times indicated. DMSO-treated cells served as control. Cells were lysed with RIPA buffer and immunoblots performed as described above. The images of the blots were quantified using ImageJ. CPSF73 expression was normalized to GAPDH and the 0 h time point. The relative expression of CPSF73 in the time course was plotted by GraphPad 8.0.

Treatment with ubiquitin and proteasome inhibitors

UBE3D KO cells were seeded at a density of 5×10^5 per well in a 6-well plate and grown in DMEM medium. On the day of the experiment, the medium was replaced with fresh medium containing MG132 (proteasome inhibitor) and TAK-243 (ubiquitin E1 ligase) with the concentrations indicated. Vehicle-treated cells served as control. Cells were lysed with RIPA and immunoblots performed as described above. The images of the blots were quantified using ImageJ. CPSF73 expression was normalized to α-Tubulin and untreated samples. The relative expression of CPSF73 was plotted by GraphPad 8.0.

RNA-sequencing Total RNA from HEK293 cells was prepared using TRIzol Reagent (Invitrogen, 15,596,018) according to manufacturer's protocol. Total RNA samples were submitted, and poly(A) selected RNAs were reversed transcribed to cDNA using random primers and used for 150bp paired end sequencing by Genewiz, Inc. For MDA-MB-231 cells, total RNA samples depleted of rRNA were converted to cDNA using random primers and 75bp paired-end stranded sequencing was done by Realseq, Inc. Three biological replicates were prepared for each sample.

Differential gene expression analysis and functional annotation Raw reads were trimmed by Cutadapt (Martin, 2011), and the quality of clean reads was evaluated with FastQC and MultiQC programs. Trimmed reads were aligned to the hg38 annotation of human genome using STAR v2.5.2b (Dobin et al., 2013). DESeq2 (Love et al., 2014) was used to analyze differential gene expression. The raw read counts were normalized using reads per kilobase of transcript per million mapped reads (RPKM). The significance of differential expression was estimated for each gene using the Wald test and then corrected for multiple comparisons using the Benjamini and Hochberg procedure (Padj). Visualization of the generated data was achieved using ggplot2 (Gómez-Rubio, 2017) and EnhancedVolcano (Blighe et al., 2022). GO enrichment analyses were performed using Metascape (https://metascape.org) (Zhou et al., 2019).

Gene readthrough analysis

downstream of Genes (DoG) transcripts were identified using DoGFinder (Wiesel et al., 2018). Differential expression analysis of normalized read counts in DoG regions was performed using DESeq2, with shrinking of log2 fold changes using ashr (Stephens, 2017), significance testing using the Wald test, and multiple-comparison correction using Benjamini and Hochberg. Visualization of the generated data was achieved using ggplot2 (Gómez-Rubio, 2017) and EnhancedVolcano (Blighe et al., 2022). Eulerr (Larsson, 2020) was used to generate proportional Venn diagrams for overlap analysis. Normalized reads maps were visualized using Jbrowse (Buels et al., 2016).

Accession numbers

RNA-seq data have been submitted to NCBI under the following GEO accession numbers: for *UBE3D* KO HEK293 samples, accession no.GEO: GSE189746; for *UBE3D* KD MDA-MB-231 samples, accession no.-GEO: GSE189723.

Transwell migration and invasion assays

For the transwell migration assays, MDA-MB-231/MDA-MB-468 cells were digested using trypsin/EDTA, and cells (4×10^4 cells) were suspended with 200 μL DMEM medium and seeded onto the upper chamber of x 24-well transwell (8 μm aperture). The lower chamber of the transwell is filled with 500 μL of DMEM medium, and the transwell incubated at 37 °C for 16 h. For migratory cell staining, transwell inserts were removed from 24-well plates and washed twice with PBS, followed by scraping off non-invaded cells on the top of the membrane with a cotton swab. The migrated cells were fixed with ice-cold methanol for 15 min and then stained with 0.2% crystal violet for 20 min. After washing with water, five pictures for each group were taken randomly under an inverted microscope. The cell numbers in each field were counted using ImageJ. Relative cell migration activities were expressed as the fold change over respective controls. Data were analyzed by GraphPad Prism 8.0. For the invasion assay, cells (8×10^4 cells) were plated on the top of chambers (Corning 3422, USA) covered by Matrigel ((ITEM: Corning Matrigel Growth Factor Reduced (GFR) Basement Membrane Matrix, LDEV-Free, 5mL, Corning 356,230)) according to the manufacturer's instructions. Briefly, Matrigel was thawed at 4 °C overnight and diluted (1:8) in cold DMEM, and 80 μL of the diluted Matrigel placed into the upper chamber of 24-well transwell (8 μm aperture) and incubated with the transwell at 37 °C for 30 min. The remaining steps of cell seeding and crystal violet staining were the same as for the migration assay.

3D invasion assay

Growth Factor Reduced BD Matrigel (140 μL) was plated on the bottom of the 24-well plate and the plate placed in the incubator for 30 min. MDA-MB-231/MDA-MB-468 cells (3×10^4 cells) were added into serum-free medium DMEM/F12 supplemented with B-27 supplement (Life Technologies, 17,504,044), 0.6% BSA, 20 ng/mL EGF (R&D Systems, 236-EG-200), 10 ng/mL FGF (R&D Systems, 233-FB-025), and 1% penicillin/streptomycin. Matrigel was added to the cells to a final concentration of 10% and the cells were plated on the top of the Matrigel layer. After cells were incubated at 37 °C for 45 min, the indicated concentrations of JTE-607 were added to the cells. Pictures were taken after 72 h of incubation and cell branches in each colony are counted.

Sphere forming assay

Single MDA-MB-231/MDA-MB-468 cells (2000 cells per well) were resuspended in serum-free DMEM/F12 medium supplemented with B-27 supplement, 0.6% BSA, 20 ng/mL EGF, 10 ng/mL FGF, and 1% penicillin/streptomycin. Matrigel was added into the cells at a volume ratio of 1:1. Cells in medium with 50% Matrigel were plated onto a 24-well ultra-low attachment plate (Corning). Covering medium and JTE-607 were refreshed every three days. After 10 days of culture, the number of spheres larger than 50 μm was counted under an inverted microscope.

Cell proliferation assay

Stable cell lines with inducible *UBE3D*/*CPSF73* shRNAs or *CPSF73* overexpression were seeded at 50,000/well in 12-well plates and treated with Dox (1.5 μg/mL) for the indicated days. Cell number was determined using Sulforhodamine B (SRB) as reported (Vichai and Kirtikara, 2006). Briefly, culture medium was removed from cell monolayers and cells were washed once with sterile PBS, followed by cell fixation with cold 10% (W/V) TCA (trichloroacetic acid) overnight at 4 °C. Cells were stained by 0.4% SRB (Sigma) in 1% acetic acid, after which cells were washed with 1% acetic acid and air dried. SRB dye was dissolved in the same amount (400 μL) of 10 mM Tris buffer (pH 10.5) in each well. The absorption of SRB in each well was read at 492 nm in a microplate reader.

Wound healing assay

MDA-MB-231 WT and *UBE3D* KD Cells were plated in a 6-well plate. After 12–24 h cultivation, cells formed a confluent monolayer and scratches were performed using a 200 μL tip, and culture medium was replaced with 100 μL fresh complete medium with or without Dox. The wound was monitored under the fluorescence microscope at the start of the experiment (t = 0 h) and after 8, 16, or 24 h of incubation. For testing the effect of JTE-607 treatment on cell migration, JTE-607 was added into the cells after the scratch at the concentration indicated.

Cell viability assay after JTE-607 treatment

For the cell viability assay in 2D cultures, MDA-MB-231/MDA-MB-468 cells were cultured in DMEM medium with 10% FBS and seeded at a density of 5×10^3 per well in 96-well plates for 24 h, and then treated with JTE-607 at the concentrations indicated. After 72 h, cell numbers were determined using SRB assay as described above. For the cell viability assay in 3D cultures, MDA-MB-231/MDA-MB-468 cells were culture in DMEM/F12 supplemented with B-27 supplement, 0.6% BSA, 20 ng/mL EGF, 10 ng/mL FGF, and 1% penicillin/streptomycin. A density of 5×10^3 cells was seeded in a 96-well ultra-low attachment plate (Corning), ATP was analyzed using CelTiter-Glo 3D Cell Viability Kit (Promega, G9681) in accordance with the manufacturer's protocol. Briefly, an equal volume of CellTiter-Glo reagent was added into each well, and the cells were incubated at room temperature in the dark. Luminescence was measured in a microplate reader.

QUANTIFICATION AND STATISTICAL ANALYSIS

Data is presented as mean, ± SD or SEM, unless otherwise stated. Two or three independent biological replicates have been performed for each experiment. Data are statistically analyzed in GraphPad Prism Software 8.0 using Student's *t* test. Detailed methods and p values are described in figure legends and individual method sections.